Tailoring the light distribution of micro-LED displays with a compact compound parabolic concentrator and an engineered diffusor

EN-LIN HSIANG,[1] ZIQIAN HE,[1] ZHIYONG YANG,[1] YI-FEN LAN,[2] AND SHIN-TSON WU[1],*

[1]*College of Optics and Photonics, University of Central Florida, Orlando, Florida 32816, USA*
[2]*AU Optronics Corp., Hsinchu Science Park, Hsinchu 300, Taiwan*
*swu@creol.ucf.edu

Abstract: We propose a novel optical design to tailor the angular distribution of a micro-LED (μLED) display system and use vehicle display as an example to illustrate the design principles. The display system consists of a μLED array with a tailored LED structure, a small formfactor compound parabolic concentrator (CPC) system, and a functional engineered diffusor. It provides high efficiency, high peak brightness, and small formfactor. In the design process, a mix-level optical simulation model, including the angular distribution of polarized emission dipole (dipole emission characteristics), Fabry-Perot cavity effect (wave optics), and light propagation process (ray optics), is established to analyze the angular distribution of μLEDs. Such an optical design process from dipole emission to display radiation pattern can be extended to other μLED display systems for different applications.

1. Introduction

Micro-light-emitting diode (μLED) with high peak brightness, true dark state, and excellent reliability is emerging as a potentially disruptive display technology [1–4]. So far, most of the development efforts are focused on μLED chip itself and manufacturing processes. For μLED chips, a great deal of endeavor is devoted to developing passivation processes [5–7] or adopting new fabrication methods [8,9] to minimize the sidewall defects, which tend to lower the quantum efficiency. In terms of manufacturing, mass transfer technology [10,11] plays a critical role to reduce the production cost. However, as μLED display technology continues to advance, the associated optical design is also crucial. Recently, μLEDs have been used in large-size TVs, vehicle displays, augmented reality (AR) and virtual reality (VR), and smart watches. Although the inherent Lambertian radiation pattern of an LED chip is attractive for wide-view TV applications [12], it is less efficient for other personal electronic devices and AR/VR projection systems. For personal electronic devices, users usually view the display screen from nearly normal direction (within ±30° for a smartphone). Therefore, a brightness enhancement film (BEF) is laminated to the LCD (liquid crystal display) backlight unit to steer the large-angle emission light toward the central area. For vehicle displays, the position between the driver's eyebox and the display panel is relatively fixed, a quasi-collimated light can also improve the brightness and light efficiency. Finally, in an AR/VR near-eye display system, our previous work [13,14] has shown that owing to the small etendue of the eye pupil, a directional emission display concentrating the display power toward the normal view greatly improves the overall system efficiency. Based on the above examples, tailoring the LED light distribution toward normal angle can improve the optical efficiency of a μLED display significantly.

In this paper, we take vehicle display as an example to illustrate the importance of optical design for μLED displays. We firstly establish a mix-level optical simulation model by considering the emission characteristics of the dipole, the Fabry-Perot cavity effect, and the light propagation

process to analyze the angular distribution of the µLEDs. Then, the tailored LED structure with desired angular intensity distribution is assembled with a compact compound parabolic concentrator (CPC) to achieve directional emission. Furthermore, a functional engineered diffusor [15] expanding the display intensity distribution in horizontal direction is implemented to meet the requirement for vehicle display applications. To further demonstrate the outstanding performance of our proposed display system, three metrics are applied: 1) Optical efficiency (η) inside the eyebox, which is the ratio of power reaching the eyebox to the total power emitted from the dipole. According to [16], a typical eyebox of instrument cluster display for drivers is ±10° in horizontal direction and -4° to 8° in vertical direction; and for passengers is ±40° in horizontal direction and -10° to 20° in vertical direction. Only the emitted light entering the eyebox of the driver or the passenger is useful. In other words, the emitted light exceeding the eyebox will not be received and is wasted. As a result, according to the Lambertian radiation pattern of normal µLED chip, a large amount of emitted light falls outside the eyebox, so that its effective optical efficiency is quite low. 2) Peak brightness in the driver's eyebox. As shown in Fig. 1(a), because of the human eye adaption [17], a vehicle display with high peak brightness (>1000 nits) is required to display information vividly under a strong ambient light environment (say, 100,000 lux). Here, to evaluate the required display brightness, we set the brightness of a white paper under different illuminances as a standard. 3) Ambient reflectance. As shown in Fig. 1(b) and 1(c), a lower ambient reflectivity helps reduce the reflected noise from the display panel to achieve a higher ambient contrast ratio (ACR) [18] under strong ambient illuminance.
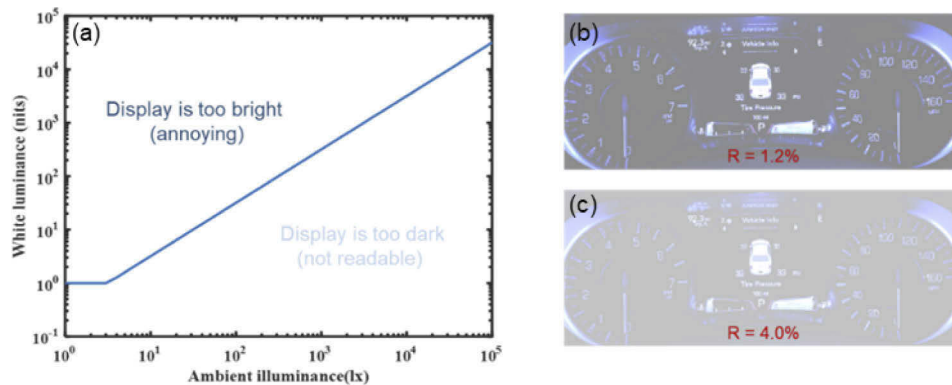

Fig. 1. (a) Typical white luminance requirements depending on ambient illuminance. Simulated displayed image of display with different ambient reflectivity (b) 1.2%, and (c) 4%. Display peak brightness: 1000 nits; ambient illuminance is 100,000 lux.

Compared to traditional µLED display, our proposed display system concentrating most of the µLED light in the eyebox region, which boosts the optical efficiency by about 2.7x and the peak brightness by more than 3x. In addition, the increased ambient contrast ratio can provide clearer images under 10,000 lux ambient illuminance. These properties further enhance the sunlight readability of µLED for automotive displays. In addition, the mix-level optical simulation model and optical design process from dipole source to display radiation pattern can be further applied to µLED display systems for other applications.

2. Device structure

2.1. GaN based µLED theoretical model

Figure 2(a) depicts the device structure of thin-film flip-chip (TFFC) LED. It consists of a high-reflectivity metal mirror, a p-GaN layer (about hundreds of nanometers), a single quantum-well

(QW) layer, and a n-GaN layer (over 4 μm) [19,20]. The radiation pattern and the polarization vector of dipole source can be represented by the azimuthal angle φ and the polar angle θ shown in Fig. 2(b). The electric field of p-polarized emission is on the same plane as the c-axis and the vector of ray propagation. On the other hand, the electric field of s-polarized emission is perpendicular to the plane and the electric field of p-wave. The anisotropic emission $(1 + \cos^2\theta)$ produced by TE component in GaN based LED is composed of an isotropic s-polarized component and a $\cos^2\theta$ p-polarized component [21]. From our previous work [22], the radiation pattern calculated by the interference theory [23–25] matches well with the simulation results by the finite-difference time-domain (FDTD) method. In both methods, the half-cavity approximation is applied, and the refractive index of GaN is 2.45 and that of Ag is $0.14 + 2.47i$, thereby the reflectivity between p-GaN and Ag is about 90%. It is worth noting that a LED with single QW is used in our simulation. In other words, the dipole is only emitted at height (h_p) above the bottom reflector. This assumption is meaningful in μLED display applications. As shown in [26], single or dual QW improves the carrier matching and achieve a higher IQE at low driving current density, which is the normal driving current for μLED displays.
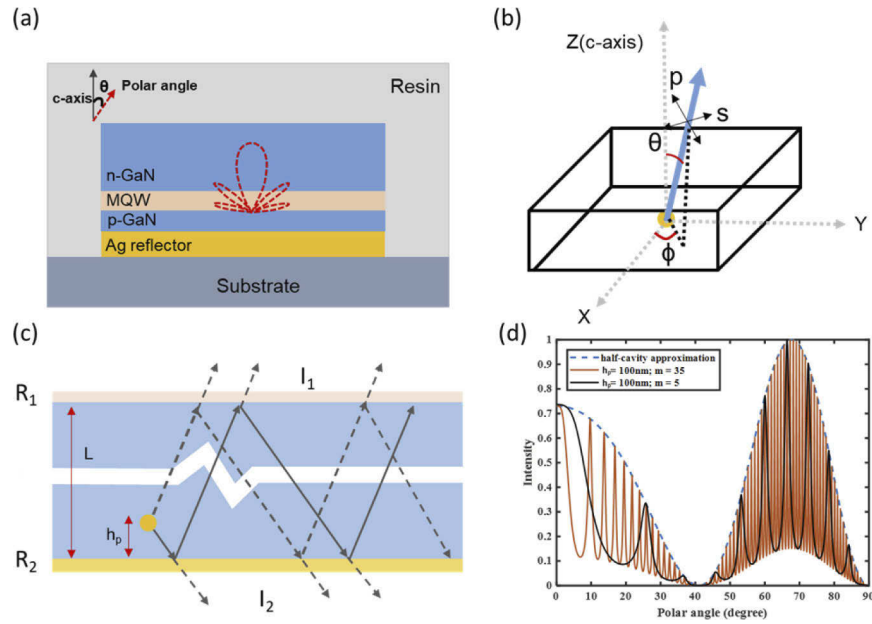

Fig. 2. (a) Schematic design of TFFC μLED chips considered in this study. (b) Schematic diagrams of coordinate system in simulation and measurement. (c) Schematic design of an emission source in a Fabry-Pérot cavity. (d) Simulated intensity distribution from the top surface of Fabry-Pérot cavity with different cavity orders.

Here, to further confirm that the half-cavity approximation is reliable, the numerical model of light source embedded in the Fabry-Pérot cavity is derived. As shown in Fig. 2(c), we consider a light source at position h_p inside the cavity and the light source emits in an isotropic manner. Again, the material inside the cavity is GaN ($n=2.45$), the bottom reflector is Ag as mentioned above, and the material above the top surface is air. The electric field emitted from the top interface is expressed as:

$$E_1 = E_0 e^{i(\phi_1 - \phi_2)} t_1 (1 + r_1 r_2 e^{2i\phi_1} + \cdots) + E_0 e^{i(\phi_1 + \phi_2)} r_2 t_1 (1 + r_1 r_2 e^{2i\phi_1} + \cdots)$$

$$= E_0 t_1 \frac{1 + r_2 e^{2i\phi_2}}{1 - r_1 r_2 e^{2i\phi_1}}; \phi_1 = n k_0 L \cos(\theta); \phi_2 = n k_0 h_p \cos(\theta), \tag{1}$$

The intensity emitted above the cavity can be further expressed as:

$$I_1 = |E_1|^2 = I_0 \frac{T_1}{(1-r_1 r_2)^2} A(\phi_1)\varsigma(\phi_2);$$

$$A(\phi_1) = \frac{1}{1+C\sin^2(\phi_1)}; C = \frac{4r_1 r_2}{(1-r_1 r_2)^2}; \varsigma(\phi_2) = 1 + R_2 + 2r_2 \cos(2\phi_2), \tag{2}$$

where r_1, r_2 is the reflection coefficient at top and bottom cavity surface, L is the cavity length, h_p is the distance from dipole to bottom reflector, and θ it the polar angle.

From Eq. (1) and Eq. (2), the intensity of a light source in a Fabry-Pérot cavity is the product of two factors: 1) Airy function:$A(\phi_1)$, which represents the resonant behavior of the Fabry-Pérot cavity, and 2) Antinode factor: $\varsigma(\phi_2)$, which indicates the coupling efficiency of the light source to the Fabry-Pérot cavity. Here, we set the distance from the dipole source to the bottom reflector as 100 nm (h_p=100 nm), and the cavity length L is set as:

$$L = \frac{m\lambda}{n_{cavity}}, \tag{3}$$

where m is the cavity order and n_{cavity} is the refractive index of the cavity. As Eq. (3) indicates, when m increases, the cavity length L increases. In other words, more modes can be supported in a thicker cavity. In addition, $R_1 \approx 0.2$ and $R_2 \approx 0.9$, is determined by Fresnel reflection at the GaN-air interface and the GaN-Ag interface, respectively. In Fig. 2(d), the cavity order is set to be 5 for a thin cavity and 35 for a thick cavity. As the cavity thickness increases, the angular intensity distribution is closer to that calculated by the half-cavity approximation method. Therefore, as long as the total cavity is thick enough ($\sim 6\,\mu$m, corresponding to the cavity order m = 35), the half-cavity approximation should be reliable, and we use it for the following LED-chip optical simulation. In addition, it is worth noting that if the MQW design is applied in the LED chip, the interference effect is not so strong as the single or dual QW [27]. Therefore, the radiation pattern of MQW µLED may not be modulated effectively by the cavity design as single or dual QW µLED. To modulate the radiation pattern of MQW µLED, additional optical structures, such as the taper angle of LED chip and extra nanostructure, are required; these are not included in the present study.

Based on the above methods, we calculated the LED's angular intensity distribution for each wavelength and polarization state (*p* or *s* component) separately, and then added them up according to their relative intensity. With various thickness of p-GaN layer, the radiation pattern changes periodically. Similar phenomenon is also observed in [28]. Then, the angular distribution is imported into the ray-tracing model in Monte Carlo LightTools [29,30] to analyze the light extraction efficiency (LEE) and the angular distribution of the LED array as shown in Fig. 2(a). The refractive index of resin is 1.5, and the absorption coefficient of GaN is 20 cm^{-1}. Other material properties remain the same as mentioned above. The emitted light inside the LED chip can be extracted to resin material by both top and lateral surfaces. In the following section, µLED array with various radiation patterns will further be implemented and optimized in different display systems, respectively.

3. System configuration

3.1. Conventional µLED display system

Figure 3 illustrates a conventional µLED display system. Here, a 20-µm×20-µm µLED is used. According to the viewing distance in a vehicle (60 cm) and human visual acuity (1/60 degree), the pixel pitch is defined as 180 µm. After transferring µLEDs to a display substrate containing predetermined thin film transistors and metal wires, a 20-µm thick resin should be used to protect the µLED. Then, black matrix is coated on top of the resin to reduce the ambient light reflected from the LED chip and the bottom metal wire. Finally, a 100-µm-thick top glass is laminated.

The window size of the black matrix should be large enough to prevent blocking the light emitted by the μLED. In order to extract all the emitted light within the critical angle, the width of the open window is defined as 56 μm [= 20 μm + 2 × H (20 μm) × tan (θ$_c$)] [31].
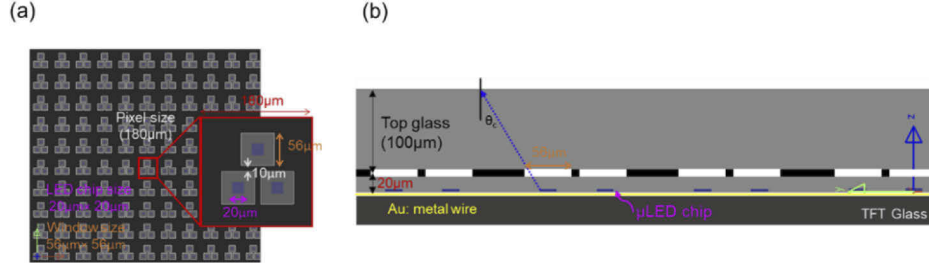

Fig. 3. Schematic diagram of conventional μLED display: (a) bird view and (b) side view.

Both light extraction efficiency and angular distribution are affected by the absorption, refraction, and reflection process in each layer. Through Monte Carol ray-tracing technique, millions of rays are traced in LightTools. In addition, the optical efficiency of a display panel is determined by several factors as follows:

$$\eta = IQE_{LED} \times LEE_{LED} \times LEE_{display} \times \beta_{collecting};$$
$$LEE_{air} = LEE_{LED} \times LEE_{display}, \tag{4}$$

where IQE_{LED} represents the internal quantum efficiency of the μLED chip, LEE_{LED} is the light extraction efficiency of the LED chip, $LEE_{display}$ is the light extraction efficiency of the display system, and $\beta_{collecting}$ is the eyebox collecting ratio defined as the power in the eyebox divided by the total power emitted from the display panel. In other words, $\beta_{collecting}$ is the ratio of the power integral in the eyebox (horizontal direction ±40°; vertical direction −10° to 20°) to the power integral in the whole emitting hemisphere. Figure 4 shows the light extraction efficiency and angular distribution of different types of μLED display in the air. By choosing p-GaN with an appropriate thickness, the LEE of μLED in the air can reach about 20% when h$_p$=225 nm. However, due to the mismatch between the eyebox (defined in Introduction) and the display radiation pattern, the optical efficiency inside the eyebox is only about 3%. Therefore, how to steer the emitted LED light toward the eyebox region is a key issue to improve the overall optical efficiency. In the present work, we do not apply surface patterning technology because it becomes more challenging as the LED size gets smaller.

3.2. Conventional CPC

CPC has been widely used to concentrate the light emitted by LEDs. Usually, the outline of CPC is comprised of two parabolas AC and BD, as shown in Fig. 5(a), where θ represents the designed maximum exit angle of the CPC element. The equivalent structure profile of CPC can be described as [32]:

$$r = \frac{-b + \sqrt{b^2 - 4ac}}{2a};$$
$$a = l^2; b = 2(lmz + r_0 n^2); c = z^2 m^2 - 2r_0 lxz - r_0^2 ny;$$
$$l = \cos(\theta); m = \sin(\theta); n = 1 + m; x = 1 + n; y = 1 + x, \tag{5}$$

where z is the height, r_0 is the radius at $z = 0$ (AB/2), and θ is the designed maximum exit angle of the CPC elements.
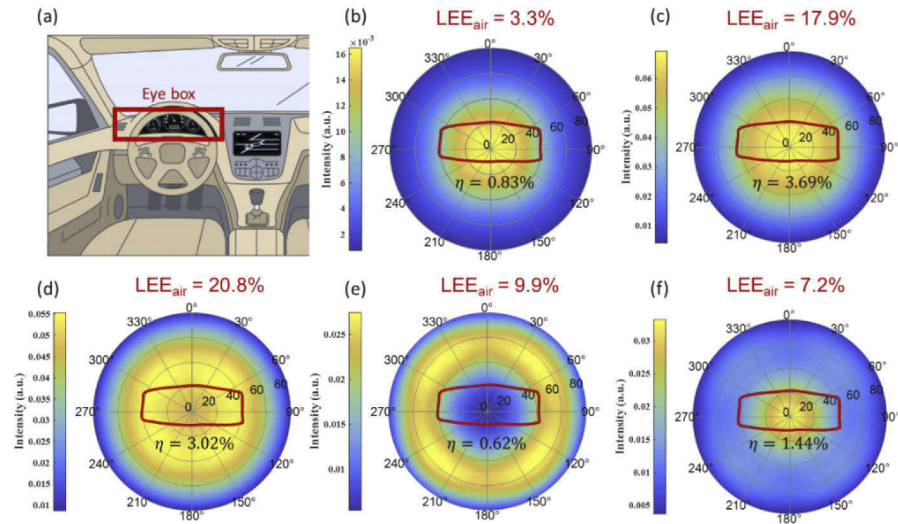
Fig. 4. (a) Schematic diagram of eyebox in a vehicle display. The angular distribution and LEE of μLED display with (b) $h_p = 175$ nm, (c) $h_p = 200$ nm, (d) $h_p = 225$ nm, (e) $h_p = 250$ nm, and (f) $h_p = 275$ nm. The red box in the figure indicates the eyebox ($\pm 40°$ horizontal and $+20°$ to $-10°$ vertical), and η is the ratio of power emitted from LED to the power reaching the eyebox area.
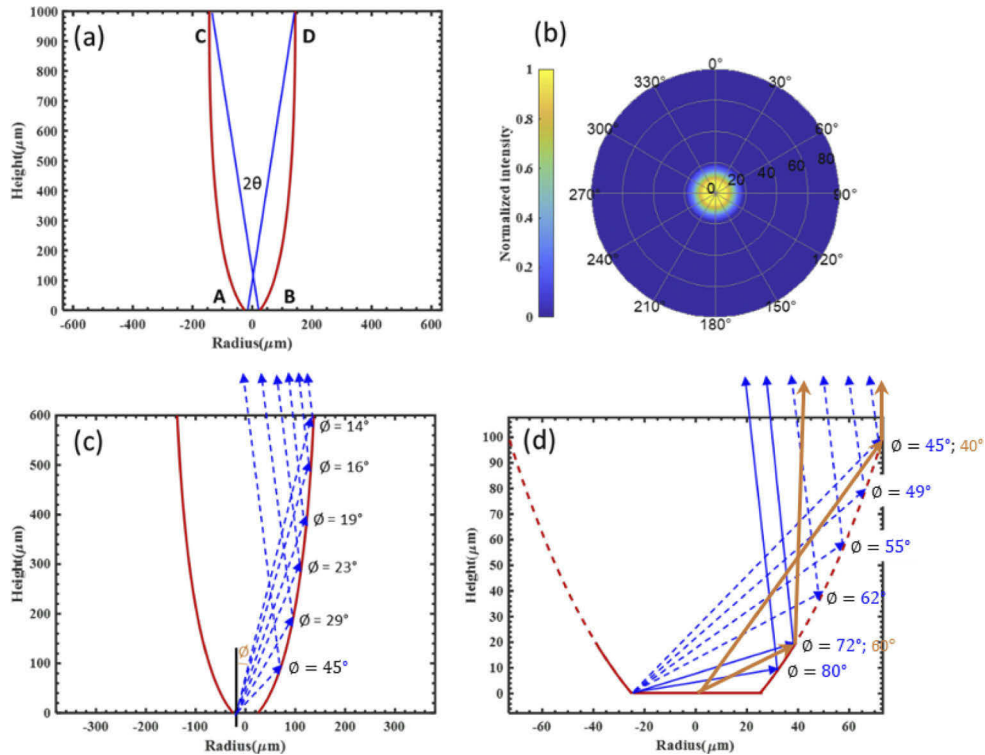

Fig. 5. (a) The 2D profile of CPC. (b) The far-field radiation pattern as a Lambertian source used in the CPC defined in (a). The 2D profile of a CPC whose height is (c) 600 μm, and (d) 100 μm.

The two-dimensional (2D) profile of a CPC with $r_0 = 25$ μm and $\theta = 10°$ is shown in Fig. 5(a). From Eq. (5), as the targeted θ gets smaller, the total thickness of CPC increases. In other words, if we want to make the emitted light more collimated, we need to use a larger CPC. It is worth noting that the refractive index of the CPC material is 1.5, which helps to reduce the total internal reflection (TIR) inside the LED chip. Considering the refraction at the CPC-air interface, the CPC with a maximum exit angle of $10°$ is enlarged to $15.1°$ ($= \sin^{-1}(1.5 \times \sin(10°))$) in the air. Here, LightTools ray-tracing simulation software is used to verify our CPC design. The Lambertian emission source with $r = 10$ μm is located at $z = 0$ in the CPC described in Fig. 5(a). The output radiation pattern in the air is measured and plotted in Fig. 5(b). Obviously, the designed CPC is a good concentrator. It can concentrate most of the light to within $15°$, which is what we designed. Although CPC is a good concentrator, its large size limits its application in high-resolution-density AR/VR displays. In addition, μLED chips are also difficult to transfer to deep cavities. Therefore, how to minimize the concentrator size is critical in μLED applications. According to the edge light principle, the light from the edge of a light source (parallel incident light with an incident angle θ) will be deflected to the edge of the receiver (point A or point B). The trajectory of the edge ray inside the CPC is shown in Fig. 5(c). To collect the emission angle ϕ from 45° to 14°, we should increase the CPC height from 100 μm to 600 μm. However, as shown in Fig. 5(d), which is an enlarged image of a CPC component with its height ranging from 0 to 100 μm, the first 100-μm height of CPC has already covered the emission angle from 90° to 45°. Therefore, if we only use CPC as a side reflector to collect light with a large emission angle, its overall size can be significantly reduced. On the other hand, if necessary, we can implement a microlens on the top surface of CPC to further collimate the light emitted at small angles.

Here, we take the CPC device drawn in Fig. 5(d) as an example. The CPC with a height of 100 μm can concentrate the emitted light with an emission angle greater than 45° to the exit angle $\theta = -10°$. Moreover, the 20-μm CPC height corresponds to an emission angle of 72°, as the emission point located at $r = -25$ μm. However, for a LED placed at the center of the CPC (emission point located at $r = 0$), the CPC height of 20 μm corresponds to an emission angle of 60° and a CPC exit angle $\theta = 0°$. Although the size is much smaller than the CPC device drawn in Fig. 5(c), the relatively deep cavity and large size still pose challenges for μLED applications. In order to solve this problem, we further reduce the CPC size by tailoring the LED radiation pattern before it enters the CPC. More specifically, we divide the LED radiant power into two major lobes. The first lobe covers from 0° to about 40°, which can be refracted to a nearly normal direction by the lens on top of the CPC element. The second lobe is from ~60° to 90°, which can be reflected toward the normal direction by the CPC. Therefore, if there is no light or the light is very weak at the emission angle from 40° to 60° (orange lines), we can apply a CPC with a merely 20-μm height (red solid line), and its performance is like a CPC with a height of 100 μm (red dashed lines). Therefore, as discussed above, we can firstly tailor the LED radiation pattern through interference inside the LED chip, and then put the customized LED into a small formfactor CPC. After that, a microlens is applied on top of the CPC element to further concentrate the emitted light toward the normal viewing direction.

3.3. Small formfactor MCPC system

According to the requirement, which demands the LED to have a weak or no emission in the 40° to 60° angular range, the p-GaN thickness of TFFC LED is tailored to 185 nm so that the destructive interference occurs at an emission angle of 24° (corresponding to 45° after interface refraction). The radiation patterns inside the LED chip and in the resin are plotted in Fig. 6(a) and 6(b), respectively. As shown in Fig. 6(b), two intensity valleys appear in the 40° to 60° range. Therefore, by carefully designing the LED device structure, we can achieve the desired LED radiation pattern. Now, the tailored LED is suitable for the compact CPC with a height of only 20 μm. As mentioned above, we can further implement a microlens on top of the CPC to

confine the emitted LED light to a small angle. Because of the additional microlens on top of the CPC, we name this device as microlens CPC (MCPC) and the schematic diagram is illustrated in Fig. 6(c). Most of the large-angle light emitted from the side of the LED chip is reflected by the CPC. On the other hand, the small-angle light emitted from the top surface is refracted by a microlens having an aperture of 47 μm, a height of 12 μm, and a front surface radius of 23 μm. Finally, the radiation pattern of the quasi-collimated light in the air is shown in Fig. 6(d). Most of the emitted light is concentrated within 30°, and the FWHM is ±18°.
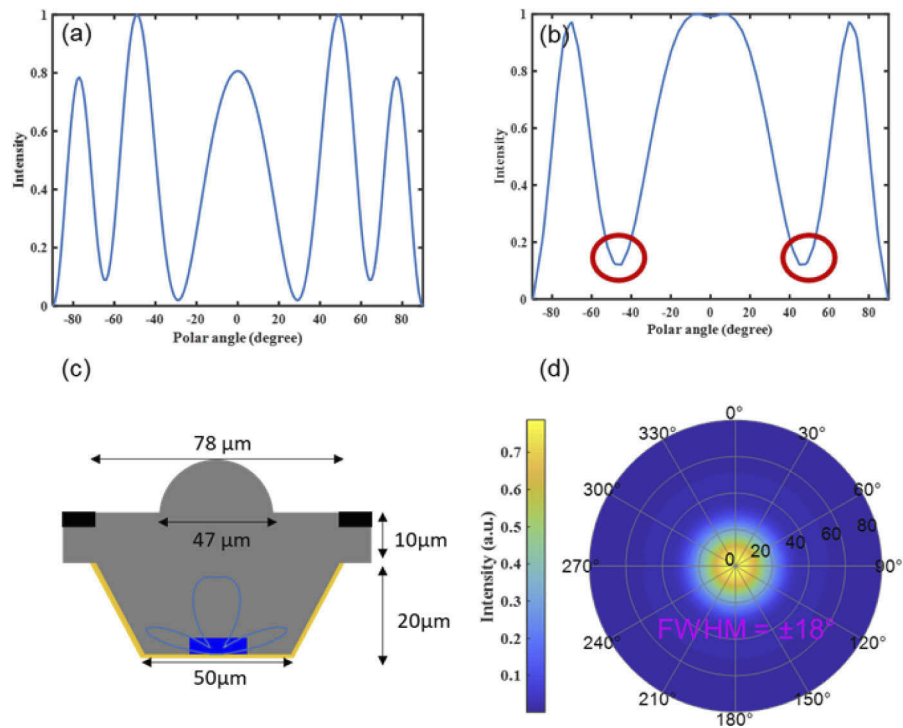

Fig. 6. The angular distribution of GaN LED with h_p = 185 nm (a) in the LED chip and (b) in the resin material. (c) The schematic diagram of MCPC. (d) The angular distribution of quasi-collimated light achieved by the small formfactor MCPC system.

3.4. Functional engineered diffusor

Although a quasi-collimated light is preferred in some handheld display applications (such as smart phones and smart watches), the rapidly decreasing intensity in the horizontal direction is undesirable for vehicle displays. Unlike a handheld display where the user can easily rotate the display to the line of sight, in a vehicle display screen, the eyebox of the driver (and passenger) is fixed. In addition, under strong ambient light conditions, the use of reflector cups may increase the ambient reflectivity and degrade the image quality. To alleviate these two problems, a functional engineered diffusor can be laminated on the bottom surface of the cover glass. As Fig. 7(a) depicts, the quasi-collimated light is focused on the top surface of the cover glass through an engineered diffusor. As a result, the sub-pixels are redefined by the black matrix on top surface of the cover glass. For simplicity yet without losing generality, we do not use the freeform design in this research. As demonstrated in [15], the freeform design engineered diffusor can achieve various radiation pattern according to the application area. Here, the refractive index of both engineered diffusor and cover glass is set to 1.7 for providing enough optical power. The

transmittance and lens power follow the Fresnel equation in the ray-tracing model. The gap between each microlens is covered by the black matrix to further reduce the optical crosstalk between pixels. In addition, the window size of each sub-pixel is set to be 80 μm × 40 μm, and the sub-pixel size is 90 μm, as depicted in Fig. 7(b). Compared to a traditional 56 μm × 56 μm μLED display, the window area is almost the same. However, here the black matrix is coated on top of the cover glass, so the surface reflectance of the glass can also be reduced. In next section, we will discuss the ambient reflectivity of these two display systems in detail. The illuminance distribution and radiation pattern of the display system are recorded by the top receiver as plotted in Fig. 7(c) and 7(d), respectively. As Fig. 7(d) shows, the quasi-collimated light is refracted into a larger polar angle in the horizontal direction by the functional engineered diffusor. Here, the functional engineered diffusor is continuous along *y*-axis, and there is no air gap or black matrix between the sub-pixels in *y* direction. As a result, the optical crosstalk in the vertical sub-pixels is about 8%. However, the crosstalk problem can be solved by disconnecting the functional engineered diffusor and the newly designed pixel arrangement. Now, let us return to the radiation pattern of Fig. 7(d). Compared to the radiation pattern of the quasi-collimated light in Fig. 6(d), the functional engineered diffusor successfully expands the light to 40° viewing angle, which is the boundary of the passenger's eyebox.
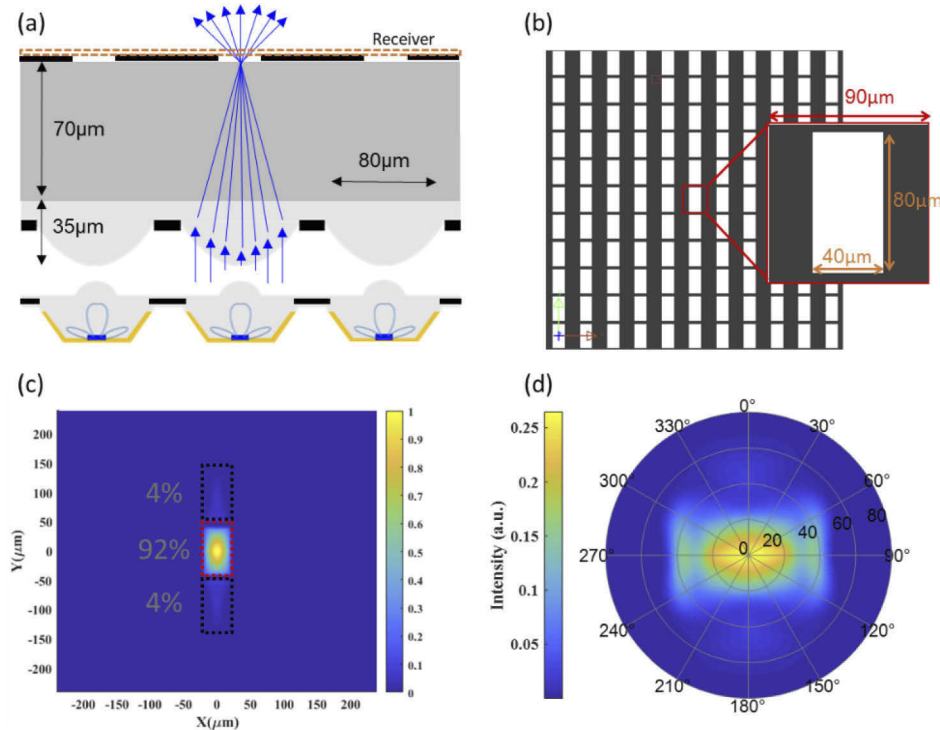

Fig. 7. Schematic diagram of our proposed μLED display: (a) side view and (b) bird view. (c) The illuminance distribution and (d) radiation pattern of the display system recorded by the top receiver.

4. Results and discussion

Here, we compare the display performance between two μLED display systems through three display metrics: optical efficiency, peak brightness, and ambient reflectivity. The μLED display system without any additional optical component as shown in Fig. 3 is called traditional display

system. Here, the thickness of p-GaN is set to be 200 nm, which corresponds to the maximum optical efficiency. On the other hand, the µLED display system shown in Fig. 7(a) is composed of the MCPC system and the functional engineered diffusor, which is referred as our proposed display system. As described above, the thickness of p-GaN is set to be 185 nm. In addition, since the size, material, structure, and LED chip size are the same, we set the *IQE* to be a uniform normalized value to facilitate the analysis. To make the comparison clearer, we redraw the radiation pattern and optical efficiency of both display systems side-by-side in Fig. 8. In our proposed display system, the MCPC redirects the light emitted from the sidewall to the normal direction, so the LEE_{air} of the display system is increased to 19.4%, which is about 8% higher than that of the traditional one. In addition, the optimized radiation pattern is concentrated in the eyebox area. As a result, the total optical efficiency (η) of the proposed display system is 2.7x (9.98÷3.69) higher than that of the traditional one.
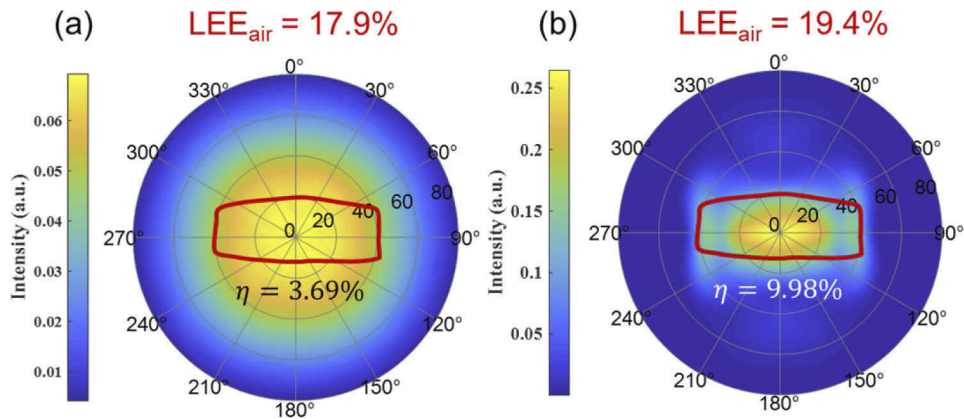

Fig. 8. Radiation pattern and optical efficiency comparison between (a) traditional display system and (b) our newly proposed display system.

The second performance metric is peak brightness. For an advanced vehicle display, the brightness in the driver's eyebox should be greater than 850 nits, while the brightness in the passenger's eyebox should be greater than 450 nits. Here, the same input power is applied to the µLED chip in the traditional and our proposed display systems. Figure 9 depicts the brightness comparison of the two systems. In the driver's eyebox area (marked by the magenta line), the maximum brightness of the proposed display system is 1150 nits, and the minimum brightness is 850 nits. Therefore, it satisfies the above-mentioned requirements in the driver's eyebox (>850 nits). In contrast, under the same input power, the maximum brightness of the traditional display system is only 312 nits, and the minimum brightness is only 267 nits. The brightness of our proposed display system is more than 3x higher than that of traditional display system. On the other hand, in the passenger's eyebox area (marked by red line), the minimum brightness of our proposed display system and traditional display system is 400 nits and 267 nits, respectively. The brightness is increased by about 1.5x. It is worth mentioning that in the proposed display system, about 99.5% of the passenger's eyebox area has brightness greater than 450 nits, which is the required value for high-end vehicle displays [16].

The third performance metric is ambient reflectivity (AR). Here, we assume no anti-glare or anti-reflection film is used. However, considering the strong ambient reflection and the relatively large LED aperture ratio (∼30%), it may be necessary to use a circular polarizer to suppress the ambient reflection from the µLED chips. The method for evaluating AR is shown in Fig. 10(a). We use the standard D65 white light source to illuminate the panel evenly from all directions while the panel is turned off. Then, the reflected brightness at each viewing angle is measured.
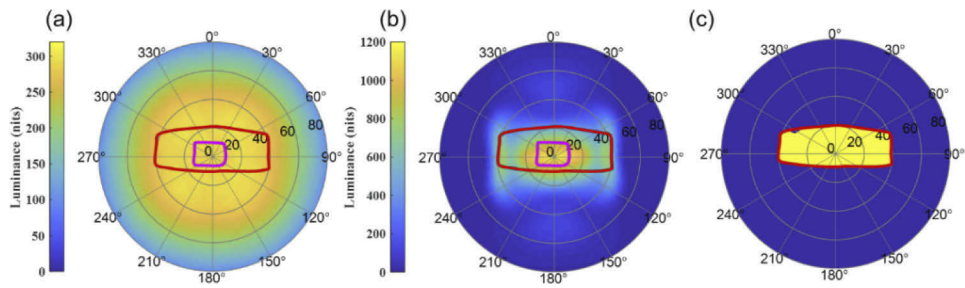
Fig. 9. Luminance comparison between (a) traditional display system and (b) our proposed display system. The magenta color box and red color box indicates the driver's and passenger's eyebox, respectively. (c) The yellow color indicates that over 99.5% area in the passenger's eyebox region has a luminance higher than 450 nits.

In addition, the AR describing how much the ambient light is reflected by the display panel is also measured from following equation:

$$AR = P_{reflec\tan ce}/P_{ambient}, \tag{6}$$

where $P_{reflectance}$ and $P_{ambient}$ stands for the reflected ambient light power and total incident ambient light power, respectively.
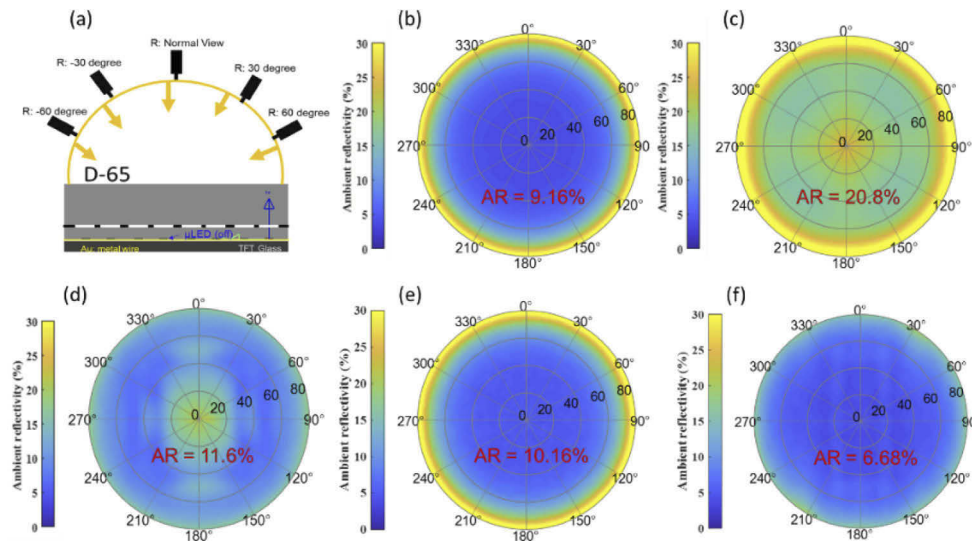

Fig. 10. (a) Schematic diagram of angular reflectivity measurement in the LightTools model. The angular reflectivity of (b) a bare glass, (c) traditional display system w/o a CP, (d) our proposed display system w/o a CP, (e) traditional display system with a CP, and (f) our proposed display system with a CP.

The ambient reflectivity of a bare glass is plotted in Fig. 10(b). Based on Fresnel reflection, a larger viewing angle suffers from a stronger ambient reflection, and the average AR of a bare glass is 9.16%. In addition, the ambient reflectivity at different viewing angles of the traditional and proposed display systems is plotted in Fig. 10(c) and 10(d), respectively. In our proposed display system, the black matrix is coated on the top (Fig. 7(a)), thus, it generally exhibits a lower AR than the traditional display system. However, as described above, in both display systems, the

aperture ratio (the ratio of the window area to the sub-pixel area) is about 40%. Therefore, some ambient light will pass through the open window, and is reflected by the bottom metal wire in the traditional system or by the reflector cup in the proposed system. Therefore, a circular polarizer (CP) is needed to eliminate this ambient reflection. Here, a conventional CP consisting of a linear polarizer and a quarter-wave plate is applied. For the quarter-wave plate, it is a 91.67-μm-thick positive A-film with $n_o = 1.5095$ and $n_e = 1.5110$ at λ=550 nm. If a broadband and wide-view CP is required, then more compensation films should be applied [33,34]. Due to the polarization effect of the employed CP, the 3D polarization ray-tracing is considered in the LightTools model so the evolution of polarization state during the optical process can be traced. The ambient reflectivity of both display systems when CP is laminated are plotted in Fig. 10(e) and 10(f). Again, because of the top black matrix, the proposed system has an even lower AR than the bare
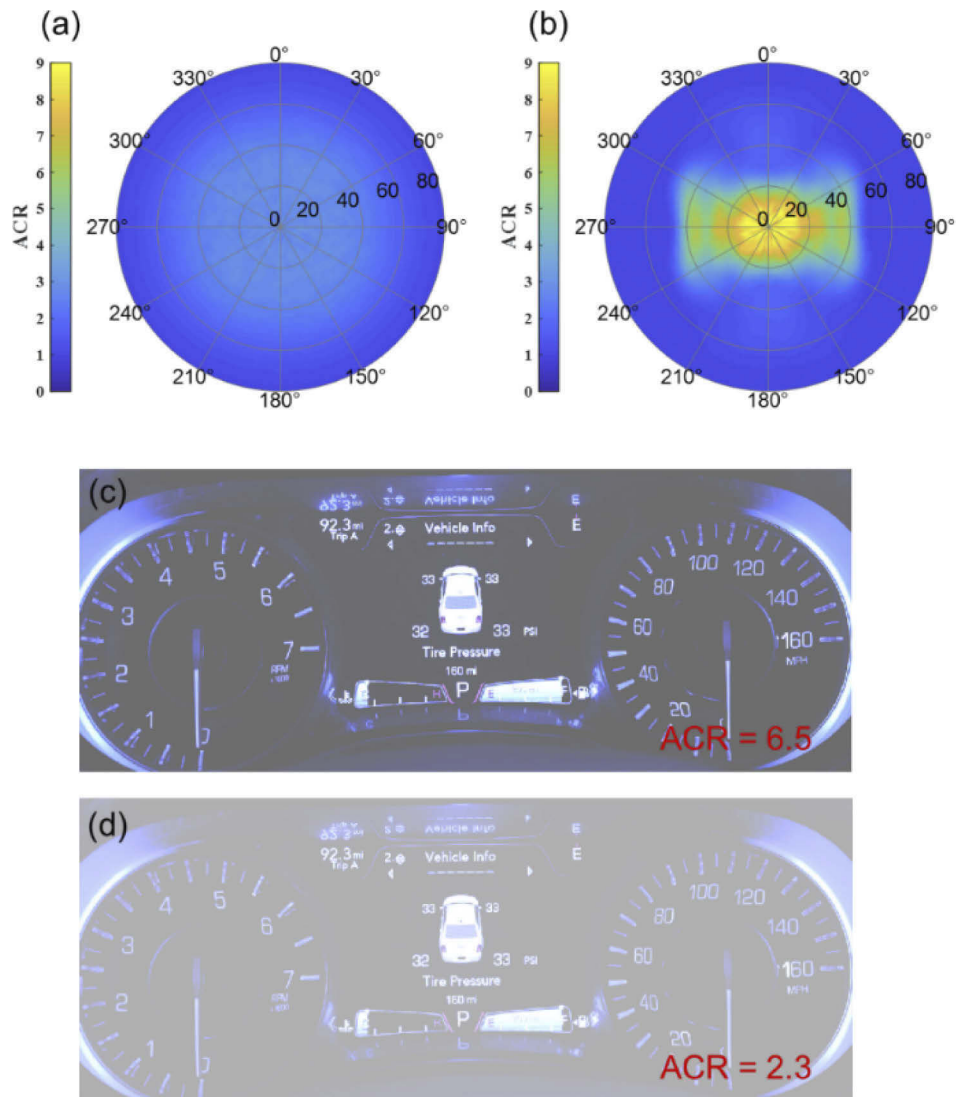

Fig. 11. Ambient contrast ratio of (a) traditional display system, and (b) proposed display system. The simulated display image of (c) proposed display system ACR = 6.5, and (d) traditional display system ACR = 2.3. The ambient illuminance is 10,000 lux.

glass. Obviously, our new display system offers a reduced ambient reflection for vehicle displays and provides clearer images under strong ambient lighting conditions.

In order to evaluate the image performance of these two display systems, we further evaluate the ACR based on the luminance distribution and ambient reflectivity. Here, the ambient illuminance is set at 10,000 lux which is approximately a daylight environment. As shown in Fig. 11(a) and 11(b), our proposed display system exhibits a higher ACR than the traditional one, indicating a better image quality. In the traditional and our proposed display systems, the minimum ACR in the driver's eyebox area is 2.3:1 and 6.5:1, respectively. The corresponding simulated images displayed by these two systems are also shown in Fig. 11(c) and 11(d) to provide a visual comparison. A higher ACR enables a faster recognition for the driver, which in turn improves the safety.

In the above-mentioned example for vehicle displays, the LED chip size is 20 μm. If we want to extend our approach to AR/VR displays, the LED chip size should be reduced to 3-5 μm. Under such condition, the size of MCPC should be proportionally reduced to about 10 μm. Although the MCPC enlarges the pixel pitch between LEDs, the resulting quasi-collimated radiation pattern can significantly improve the light collection efficiency of the micro-LED light engine [4]. Therefore, a higher peak brightness can be achieved to keep a decent ACR for AR displays under strong ambient lighting condition. Compared to a large size (~100 μm) MCPC, the reduced microlens size may cause a non-negligible diffraction effect.

Moreover, in the above discussion we only focus on GaN-based blue LEDs. To achieve a full-color display, we also need green and red LEDs. For the GaN-based green LEDs, we only need to modulate the thickness of the LED cavity, such as h_p, to obtain a similar radiation pattern. In comparison with a blue LED ($\lambda=450\,nm$) that achieves the target radiation pattern at $h_p=185\,nm$, the longer-wavelength green LED ($\lambda=530\,nm$) results in a larger h_p (225 nm) to generate the same radiation pattern. For the red LED, if it is also made by GaN material, then the same characteristics can be maintained. However, if the red LED is based on GaP material whose refractive index (n~3) is much higher than that of GaN (n~2.45), then the above-mentioned design process needs to be further optimized.

5. Conclusion

We have investigated the optical properties of a new μLED display through the mix-level optical simulation model, including the angular distribution of polarized emission dipole (dipole emission characteristics), Fabry-Perot cavity effect (wave optics), and light propagation process (ray optics). Benefiting from the interference effect in the Fabry-Pérot cavity, a quasi-collimated light can be achieved, and the compact MCPC system is promising for direct-view displays. Afterwards, a functional engineered diffusor is designed to tailor the angular distribution of the quasi-collimated light to fit the driver's eyebox for vehicle displays. To compare against the three display performance metrics, our proposed μLED display system exhibits a 2.7x higher optical efficiency, 3x higher peak brightness, and 2.8x higher ACR under 10,000 lux ambient illuminance. A better sunlight readability helps the drivers to get faster recognition, which could significantly improve the driving safety.

Disclosures. The authors declare no conflicts of interest.

Data availability. Data underlying the results presented in this paper are not publicly available at this time but may be obtained from the authors upon reasonable request.

References

1. J. Y. Lin and H. X. Jiang, "Development of microLED," Appl. Phys. Lett. **116**(10), 100502 (2020).
2. M. S. Wong, S. Nakamura, and S. P. DenBaars, "Review—progress in high performance III-nitride micro-light-emitting diodes," ECS J. Solid State Sci. Technol. **9**(1), 015012 (2020).

3. Y. Huang, E. L. Hsiang, M. Y. Deng, and S. T. Wu, "Mini-LED, Micro-LED and OLED displays: present status and future perspectives," Light: Sci. Appl. **9**(1), 105 (2020).
4. J. Xiong, E. L. Hsiang, Z. He, T. Zhan, and S. T. Wu, "Augmented reality and virtual reality displays: emerging technologies and future perspectives," Light: Sci. Appl. **10**(1), 216 (2021).
5. M. S. Wong, C. Lee, D. J. Myers, D. Hwang, J. A. Kearns, T. Li, J. S. Speck, S. Nakamura, and S. P. DenBaars, "Size-independent peak efficiency of III-nitride micro-light-emitting-diodes using chemical treatment and sidewall passivation," Appl. Phys. Express **12**(9), 097004 (2019).
6. Y. Boussadi, N. Rochat, J. P. Barnes, B. B. Bakir, P. Ferrandis, B. Masenelli, and C. Licitra, "Investigation of sidewall damage induced by reactive ion etching on AlGaInP MESA for micro-LED application," J. Lumin. **234**, 117937 (2021).
7. S. W. H. Chen, C. C. Shen, T. Wu, Z. Y. Liao, L. F. Chen, J. R. Zhou, C. F. Lee, C. H. Lin, C. C. Lin, C. W. Sher, P. T. Lee, A. J. Tzou, Z. Chen, and H. C. Kuo, "Full-color monolithic hybrid quantum dot nanoring micro light-emitting diodes with improved efficiency using atomic layer deposition and nonradiative resonant energy transfer," Photonics Res. **7**(4), 416–422 (2019).
8. J. Park, J. H. Choi, K. Kong, J. H. Han, J. H. Park, N. Kim, E. Lee, D. Kim, J. Kim, D. Chung, and S. Jun, "Electrically driven mid-submicrometre pixelation of InGaN micro-light-emitting diode displays for augmented-reality glasses," Nat. Photonics **15**(6), 449–455 (2021).
9. S. Lee, J. Kim, J. Oh, J. Ryu, K. Hwang, J. Hwang, S. Kang, J. H. Choi, Y. C. Sim, Y. H. Cho, and T. H. Chung, "A discrete core-shell-like micro-light-emitting diode array grown on sapphire nano-membranes," Sci. Rep. **10**(1), 7506 (2020).
10. B. Corbett, R. Loi, W. Zhou, D. Liu, and Z. Ma, "Transfer print techniques for heterogeneous integration of photonic components," Prog. Quantum Electron. **52**, 1–17 (2017).
11. R. S. Cok, M. Neitl, R. Rotzoll, G. Melnik, A. Fecioru, A. J. Trindade, B. Raymond, S. Bonafede, D. Gomez, T. Moore, C. Prevatte, E. Radauscher, S. Goodwin, P. Hines, and C. A. Bower, "Inorganic light-emitting diode displays using micro-transfer printing," J. Soc. Inf. Disp. **25**(10), 589–609 (2017).
12. G. Biwa, A. Aoyagi, M. Doi, K. Tomoda, A. Yasuda, and H. Kadota, "Technologies for the Crystal LED display system," J. Soc. Inf. Disp. **29**(6), 435–445 (2021).
13. T. Zhan, E. L. Hsiang, K. Li, and S. T. Wu, "Enhancing the Optical Efficiency of Near-Eye Displays with Liquid Crystal Optics," Crystals **11**(2), 107 (2021).
14. J. Zou, T. Zhan, E. L. Hsiang, X. Du, X. Yu, K. Li, and S. T. Wu, "Doubling the optical efficiency of VR systems with a directional backlight and a diffractive deflection film," Opt. Express **29**(13), 20673–20686 (2021).
15. R. Zhu, Q. Hong, Y. Gao, Z. Luo, S. T. Wu, M. C. Li, S. L. Lee, and W. C. Tsai, "Tailoring the light distribution of liquid crystal display with freeform engineered diffuser," Opt. Express **23**(11), 14070–14084 (2015).
16. K. Blankenbach, "Advanced automotive display measurements: Selected challenges and solutions," J. Soc. Inf. Disp. **26**(9), 517–525 (2018).
17. S. K. Nayar and M. Oren, "Visual appearance of matte surfaces," Science **267**(5201), 1153–1156 (1995).
18. J. H. Lee, X. Zhu, Y. H. Lin, T. C. Lin, H. C. Hsu, H. Y. Lin, and S. T. Wu, "High ambient-contrast-ratio display using tandem reflective liquid crystal display and organic light-emitting device," Opt. Express **13**(23), 9431–9438 (2005).
19. M. R. Krames, O. B. Shchekin, R. Mueller-Mach, G. O. Mueller, L. Zhou, G. Harbers, and M. G. Craford, "Status and future of high-power light-emitting diodes for solid-state lighting," J. Disp. Technol. **3**(2), 160–175 (2007).
20. P. Zhu and N. Tansu, "Resonant cavity effect optimization of III-nitride thin-film flip-chip light-emitting diodes with microsphere arrays," Appl. Opt. **54**(20), 6305–6312 (2015).
21. X. Chen, C. Ji, Y. Xiang, X. Kang, B. Shen, and T. Yu, "Angular distribution of polarized light and its effect on light extraction efficiency in AlGaN deep-ultraviolet light-emitting diodes," Opt. Express **24**(10), A935–A942 (2016).
22. E. L. Hsiang, Y. Li, Z. He, T. Zhan, C. Zhang, Y. F. Lan, Y. Dong, and S. T. Wu, "Doubling the optical efficiency of color-converted micro-light-emitting diode displays with a patterned cholesteric liquid crystal polymer film," J. Soc. Inf. Disp. **29**(5), 288–297 (2021).
23. P. Zhao and H. Zhao, "Analysis of light extraction efficiency enhancement for thin-film-flip-chip InGaN quantum wells light-emitting diodes with GaN micro-domes," Opt. Express **20**(S5), A765–A776 (2012).
24. H. Benisty, H. De Neve, and C. Weisbuch, "Impact of planar microcavity effects on light extraction-Part I: Basic concepts and analytical trends," IEEE J. Quantum Electron. **34**(9), 1612–1631 (1998).
25. Y. C. Shen, J. J. Wierer, M. R. Krames, M. J. Ludowise, M. S. Misra, F. Ahmed, A. Y. Kim, G. O. Mueller, J. C. Bhat, S. A. Stockman, and P. S. Martin, "Optical cavity effects in InGaN/GaN quantum-well-heterostructure flip-chip light-emitting diodes," Appl. Phys. Lett. **82**(14), 2221–2223 (2003).
26. S. Lu, J. Li, K. Huang, G. Liu, Y. Zhou, D. Cai, R. Zhang, and J. Kang, "Designs of InGaN Micro-LED Structure for Improving Quantum Efficiency at Low Current Density," Nanoscale Res. Lett. **16**(1), 99 (2021).
27. L. Wang, J. Sun, Q. Yan, J. Lin, W. Guo, E. Chen, C. Xu, and Y. Liu, "Issue of spatial coherence in MQW based micro-LED simulation," Opt. Express **29**(20), 31520–31526 (2021).
28. H. Y. Ryu, J. Pyo, and H. Y. Ryu, "Light Extraction Efficiency of GaN-Based Micro-Scale Light-Emitting Diodes Investigated Using Finite-Difference Time-Domain Simulation," IEEE Photonics J. **12**(2), 1–10 (2020).
29. Z. Liu, K. Wang, X. Luo, and S. Liu, "Precise optical modeling of blue light-emitting diodes by Monte Carlo ray-tracing," Opt. Express **18**(9), 9398–9412 (2010).

30. F. Gou, E. L. Xiang, G. Tan, P. T. Chou, Y. L. Li, Y. F. Lan, and S. T. Wu, "Angular color shift of micro-LED displays," Opt. Express **27**(12), A746–A757 (2019).
31. J. Ho and G. Biwa, "Display device and light-emitting element," U.S. patent 10,231,294B2 (12 March 2019).
32. S. Thiele, T. Gissibl, H. Giessen, and A. M. Herkommer, "Ultra-compact on-chip LED collimation optics by 3D femtosecond direct laser writing," Opt. Lett. **41**(13), 3029–3032 (2016).
33. Q. Hong, T. X. Wu, R. Lu, and S. T. Wu, "A wide-view circular polarizer consisting of a linear polarizer and two biaxial films," Opt. Express **13**(26), 10777–10782 (2005).
34. S. W. Oh, S. H. Kim, J. M. Baek, and T. H. Yoon, "Design of an achromatic wide-view circular polarizer using normal dispersion films," J. Inf. Disp. **20**(1), 25–30 (2019).